Mon. Not. R. Astron. Soc. **000**, 000–000 (0000) Printed 9 February 2022 (MN LATEX style file v2.2)

Kinematics of solid particles in a turbulent protoplanetary disc

Augusto Carballido[1],⋆ James M. Stone[2],† Neal J. Turner[1] ‡
[1] *Jet Propulsion Laboratory, MS 169-506, California Institute of Technology, Pasadena CA 91109, USA*
[2] *Department of Astrophysical Sciences, Princeton University, Princeton NJ 08544, USA*

9 February 2022

ABSTRACT

We perform numerical simulations of solid particle motion in a shearing box model of a protoplanetary disc. The accretion flow is turbulent due to the action of the magnetorotational instability. Aerodynamic drag on the particles is modelled using the Epstein law with the gas velocity interpolated to the particle position. The effect of the magnetohydrodynamic turbulence on particle velocity dispersions is quantified for solids of different stopping times $t_{\rm s}$, or equivalently, different sizes. The anisotropy of the turbulence is reflected upon the dispersions of the particle velocity components, with the radial component larger than both the azimuthal and vertical components for particles larger than ~ 10 cm (assuming minimum-mass solar nebula conditions at 5 AU). The dispersion of the particle velocity magnitude, as well as that of the radial and azimuthal components, as functions of stopping time, agree with previous analytical results for isotropic turbulence. The relative speed between pairs of particles with the same value of $t_{\rm s}$ decays faster with decreasing separation than in the case of solids with different stopping time. Correlations in the particle number density introduce a non-uniform spatial distribution of solids in the 10 to 100 cm size range. Any clump of particles is disrupted by the turbulence in less than one tenth of an orbital period, and the maximally concentrated clumps are stable against self-gravitational collapse.

Key words: accretion, accretion discs – Solar system: formation – planetary systems: protoplanetary discs – MHD – turbulence

1 INTRODUCTION

In order for planetesimals to form in a circumstellar disc, the parent dust grains must meet a variety of kinematic conditions if they are to grow in mass and size. The formation of kilometre-sized solid bodies by gravitational instability requires, through the Toomre criterion, that the dust spatial density be $\rho_d > \Omega^2/\pi G$, where Ω is the disc angular velocity and G the gravitational constant. Such densities could be achieved in a mid-plane dust layer after sedimentation has occurred. On the other hand, growth by collisional sticking may be accomplished if the grain relative speeds acquire certain values: experiments have shown that, for micron-sized grains, collision speeds less than $\sim$0.2 m/s lead to aggregates with a fractal geometry (Blum & Wurm 2000), and above $\sim$ 1 m/s disruption of the colliding agglomerates takes place.

While binary collisions of the smallest dust grains are caused by Brownian motion, other sources of relative velocities in a protoplanetary nebula may come into play as the interaction between solids and gas decreases. Differential sedimentation, radial drift and turbulence can provide the necessary kinetic energies to drive the collisional motion of solids, in addition to changing their spatial distribution throughout the nebular disc. In this paper we focus on the effect of a turbulent gas flow on solid particle velocities and spatial arrangement.

The formalism of Völk et al. (1980) makes it possible to calculate the velocity dispersions of particles in isotropic turbulence. The effect of the fluctuating gas velocity on individual solids is approximated by a sum over two types of turbulent eddies: those with spatial frequencies k and turnover times $t_k > t_{\rm s}$, where $t_{\rm s}$ is the particle stopping time, and which merely advect the particle; and those with $t_k < t_{\rm s}$, which decay before the particle has had time to cross them. The result is a velocity dispersion that decreases with particle stopping time as $(\Omega t_{\rm s})^{-1/2}$, with a sharp steepening for particles with $\Omega t_{\rm s} \sim$ a few times 10^{-1}. Under minimum mass solar nebula conditions at 5 AU, this corresponds to parti-

⋆ E-mail: augusto@jpl.nasa.gov
† E-mail: jstone@astro.princeton.edu
‡ E-mail: neal.turner@jpl.nasa.gov

cle radii of tens of centimetres. The method is nicely summarised and applied by Cuzzi & Hogan (2003) to chondrule-sized objects.

The accumulation of a large number of solids in small regions of the turbulent protoplanetary disc can lead to feedback effects on the gas flow if the solid mass density is greater than the local gas density. Such particle agglomerations can also lead to dust growth if the associated collision rates are conducive to sticking. One recently suggested clumping mechanism is a streaming instability that arises due to the relative motion between solids and gas in a Keplerian disk (Youdin & Goodman 2005). The feedback of solids onto the gas can generate exponential growth of particle density perturbations as well as turbulence, and particle clumps can develop overdensities up to a factor of ~ 50 relative to the mean gas density (Youdin & Johansen 2007, Johansen & Youdin 2007).

The process of turbulent concentration (Maxey 1987) has been explored by Cuzzi et al. (2001), who use the ratio of local particle density to its global average as the measure of a multifractal distribution of concentrated chondrules. This distribution resembles that of the dissipation of the turbulent kinetic energy on the Kolmogorov scale (Chhabra 1989). The connection between turbulent concentration and turbulent dissipation suggests that the local structure of the chondrule concentration field may be independent of flow properties. For larger particles, an accurate characterisation of their number statistics in the turbulent circumstellar environment is still lacking.

The recognition that turbulence due to the magnetorotational instability (MRI; Balbus & Hawley 1991; Hawley, Gammie & Balbus 1995, henceforth HGB) can provide the viscous stresses necessary to allow inward accretion in discs, has prompted investigations of different dynamical aspects of dust evolution in the presence of magnetohydrodynamic (MHD) turbulence. Planetesimal formation by gravitational instability was addressed by Johansen et al. (2006, henceforth JKH), whose numerical studies concluded that groups of at least 1000 particles in their simulations could become gravitationally bound, assuming specific values of disc column densities (150 and 900 g cm^{-2}) and a ratio of disc scale height to radius of 0.04. Fromang & Nelson (2005) examine the accumulation of individual solids due to vortical structures in a global protoplanetary disc model. They follow the radial migration of up to 3000 bodies, whose drag interaction with the gas corresponds to objects of approximately 1 m in size. Those particles able to migrate inwards do so at different rates, with reductions in semi-major axes ranging from a factor of 1.6 in approximately 50 orbits to a factor of 2.2 in 200 orbits. The particles that become trapped in vortices maintain an approximate constant radial position until the end of the simulation.

In the following we present a study of the kinematics of solid particles in a local MHD model of a protoplanetary disc. In Section 2 we describe the numerical method employed to model the accretion flow and the particles. Section 3 contains results obtained from measurements of particle velocities and spatial distribution. In Section 4 we discuss their significance in the context of particle growth in a protoplanetary nebula, and concluding remarks are presented in Section 5.

2 METHOD

2.1 Numerical Method

We use a three-dimensional version of the ZEUS code (Stone & Norman 1992a;b) in which the shearing box model of HGB is implemented. To simulate the solid particles, we have added a module that solves their equation of motion,

$$\mathbf{f} = -\frac{\mathbf{1}}{\mathrm{t_s}}(\mathbf{v}_\mathrm{p} - \mathbf{v}_\mathrm{g}) - 2\boldsymbol{\Omega} \times \mathbf{v}_\mathrm{g} + 3\Omega^2 \mathrm{x}\hat{\mathbf{x}} \tag{1}$$

where $\mathbf{f}$ is the force per unit mass on the particle, the first term on the right-hand side is the Epstein drag law for spherical particles, t_s is the particle stopping time, $\mathbf{v}_\mathrm{p}$ is the particle velocity, $\mathbf{v}_\mathrm{g}$ is the velocity of the background flow at the particle's position, and $\boldsymbol{\Omega} = (0, 0, \Omega)$ is the angular velocity of the box. The last two terms of Eq. (1) are the Coriolis and tidal forces, respectively, that arise as a result of the non-inertial character of the shearing box (x is the distance in the radial direction $\hat{\mathbf{x}}$). The particle module takes as input the gas velocities $\mathbf{v}$ calculated by ZEUS on the faces of the computational grid cells. These velocities are obtained by solving the ideal MHD equations for the shearing box, together with an isothermal equation of state,

$$\frac{\partial \rho_\mathrm{g}}{\partial t} + \nabla \cdot (\rho_\mathrm{g} \mathbf{v}) = 0 \tag{2}$$

$$\frac{\partial \mathbf{v}}{\partial t} + \mathbf{v} \cdot \nabla \mathbf{v} = -\frac{1}{\rho_\mathrm{g}} \nabla \left(P + \frac{B^2}{8\pi} \right) + \frac{(\mathbf{B} \cdot \nabla)\mathbf{B}}{4\pi\rho_\mathrm{g}} - 2\boldsymbol{\Omega} \times \mathbf{v} + 3\Omega^2 \mathrm{x}\hat{\mathbf{x}} \tag{3}$$

$$\frac{\partial \mathbf{B}}{\partial t} = \nabla \times (\mathbf{v} \times \mathbf{B}) \tag{4}$$

$$P = \rho_\mathrm{g} c_\mathrm{s}^2 \tag{5}$$

where ρ_g is the gas density, $\mathbf{B}$ is the magnetic field, P is the gas pressure, and c_s is the isothermal sound speed. The module interpolates each velocity component to the position of each particle inside the respective computational grid cell, using a trilinear interpolation algorithm (Press et al. 1992). Equation (1) is solved via a second-order Runge-Kutta method. The back reaction of the particles on the gas, inter-particle interactions, and particle coupling to the magnetic field are not included.

Despite the likely presence of dead zones in protoplanetary discs as a result of non-ideal MHD processes (Gammie 1996), in this first study we neglect the effect of resistivity and assume that our local disc model represents an active region in the surface layers or at a large orbital radius (Sano et al. 2000).

We adopt the values used in HGB for the initial density, initial pressure, angular velocity, plasma parameter and box dimensions: $\rho_0 = 1$, $P_0 = 10^{-6}$, $c_\mathrm{s} = \Omega = 10^{-3}$, $\beta = 400$ and $H \times 2\pi H \times H$ (where H is the disc scale height), respectively. The initial magnetic field is vertical but, unlike HGB, it varies sinusoidally in the radial direction, in such a way that the net magnetic flux is zero. The grid resolution used is $84 \times 180 \times 84$ zones.

Simple tests of the particle integrator involved the evolution of a single solid particle in a zero-velocity background flow, with various values of the stopping time $t_{\rm s}$ which, in the Epstein regime, is given by (Weidenschilling 1977).

$$t_{\rm s} = \frac{a\rho_{\rm p}}{c_{\rm s}\rho_{\rm g}} \tag{6}$$

where a is the particle radius and $\rho_{\rm p}$ the particle solid density. Given an initial position and velocity, the response time of the particle to the drag force was found to adjust accurately to the expected analytical behaviour for a range of values of the dimensionless stopping time $\Omega t_{\rm s}$ between $2{\times}10^{-3}$ and 100.

2.2 Simulations

We performed two sets of simulations in which the shearing box is first evolved for 10 orbits (1 orbit=$2\pi/\Omega$) to ensure that turbulence due to the MRI has developed. At this time, N particles are introduced in the flow with random initial positions and with initial velocities set to zero. In simulation set A, $N = 80,000$, and the total number of particles is divided in eight groups of 10,000 members. Each group is given a specific value of $\Omega t_{\rm s}$. The values used were 100, 30, 10, 5, 2, 0.2, 0.02 and 0.002. The system was evolved for a further 100 orbits.

Simulation set B, which was used to study the particle spatial distribution, consists of four groups of $N = 4,704,000$ particles, with each group having one of $\Omega t_{\rm s}$=2, 0.2, 0.125 and 0.05. The code was run for a further 30 orbits.

3 RESULTS

3.1 Viscous evolution of disc

Figure 1 shows the evolution of the magnetic (*dotted line*) and hydrodynamic (*dashed line*) volume-averaged stresses associated with our disc model, during the longest run performed. The stresses are normalized to the initial pressure. Their sum (*solid line*) gives an estimate of the volume-averaged α parameter of classical disc theory. The average value of α is 8×10^{-3}, which falls in the range $10^{-4}-10^{-2}$ inferred for T Tauri stars (e.g. Hartmann et al. 1998).

3.2 Velocity dispersions

Simulation set A has been used to calculate the time-averaged distributions of the particle velocity components. The resulting dispersions, $\sigma^{\rm p}_{v_i}$ $(i = x, y, z)$, normalised by the corresponding gas velocity dispersions $\sigma^{\rm g}_{v_i}$, have been measured as functions of particle stopping time. To calculate this ratio, $S_i \equiv \sigma^{\rm p}_{v_i}/\sigma^{\rm g}_{v_i}$, the gas velocities were computed at the position of the particles, at each snapshot and for each value of $\Omega t_{\rm s}$, and the effect of shear was subtracted from the particle and gas y-velocities. The ratios S_i thus obtained were then averaged over the last 10 orbits of the simulation, a period in which the largest particles (those with $\Omega t_{\rm s}$=100) have reached dynamical equilibrium with the gas.

The results are summarised in Fig. 2, where the solid-to-gas ratios of the x (*squares*), y (*triangles*) and z (*filled circles*) components of the velocity dispersions are plotted. Also shown as plus signs are the ratios $S_v \equiv \sigma^{\rm p}_v/\sigma^{\rm g}_v$ of the velocity magnitude dispersions $\sigma^{\rm p,g}_v = \sqrt{\langle(v_{\rm p,g} - \langle v_{\rm p,g}\rangle)^2\rangle}$ (notice that $S_v^2 \neq S_x^2 + S_y^2 + S_z^2$). The dotted curve corresponds to the analytical solution of Völk et al. (1980) and Cuzzi et al. (1993) for S_v. The solid and dashed curves correspond, respectively, to the radial and azimuthal solutions of Youdin and Lithwick (2007). With no gas drag, the particles would follow epicyclic paths with the ratio $\sigma^{\rm p}_{v_x}/\sigma^{\rm p}_{v_y}$ of the radial and azimuthal velocity dispersions equal to 2. Larger ratios $\sigma^{\rm p}_{v_x}/\sigma^{\rm p}_{v_y}$ of around 2.3 measured in the MHD calculation are due to weak drag forces from the turbulence. Separate numerical integration of the particle equation of motion (1) with a sinusoidally time-varying gas velocity reproduces the anisotropy, given variation periods of one to two orbits. Fourier analysis of the gas velocities at the particle locations in the MHD calculation indicates the strongest modes do have periods longer than one orbit. Our neglect of the vertical component of gravity appears to have little effect on the ratios between particle velocity components, as similar anisotropy was observed in stratified shearing box calculations (Carballido et al. 2006), in which for the $\Omega t_{\rm s}$=10 case, $\sigma^{\rm p}_{v_x} \sim 2.5\sigma^{\rm p}_{v_z}$.

It is important to remark that the analytical models of Fig. 2 were originally derived assuming an isotropic turbulent velocity field, so in principle one should not expect that they be an accurate description of particle motion in MRI turbulence. Nevertheless, the particle data obtained from the simulations conform reasonably well to the models. This will be discussed below.

3.3 Pair-wise relative velocities

Fig. 3 shows the magnitude $v_{\rm rel}$ of the relative velocity of pairs of particles that are located inside a cubic sub-volume in the box, in simulation set A, as a function of inter-particle separation r (in units of the box size H). The velocity has been normalised to the gas sound speed. The sub-volume has dimensions $1\times1\times1$, and extends along the y direction between the values $y = 2.64$ and $y = 3.64$. At each snapshot, a sample of 700 particles, all with the same stopping time, is randomly selected in the sub-volume, and the relative speed for each of the 244,650 possible pairs in the sample is calculated. The relative separation between pair members is binned, with the bin size equal to the x-length of a grid cell. The values of $v_{\rm rel}$ are then averaged in each bin over a duration of 7 orbits. The data shown correspond to the stopping times $\Omega t_{\rm s}$=100 (*triangles*), 10 (*squares*), 0.2 (*diamonds*), and $2{\times}10^{-3}$ (*filled circles*). To calculate $v_{\rm rel}$, the contribution of the shear has been subtracted from the y component of the particle velocities.

It can be seen that at small separations the relative speed decreases appreciably. This is to be expected, since grains that are equally coupled to the gas move coherently with small turbulent eddies. In the limit of particle stopping times less than the lifetime of the smallest eddies, the laminar flow on scales below the dissipation scale does not contribute to the random relative grain velocity. Formally, this can be expressed for grains of stopping times $t_{\rm s_1}$ and $t_{\rm s_2}$ as (Weidenschilling 1984)

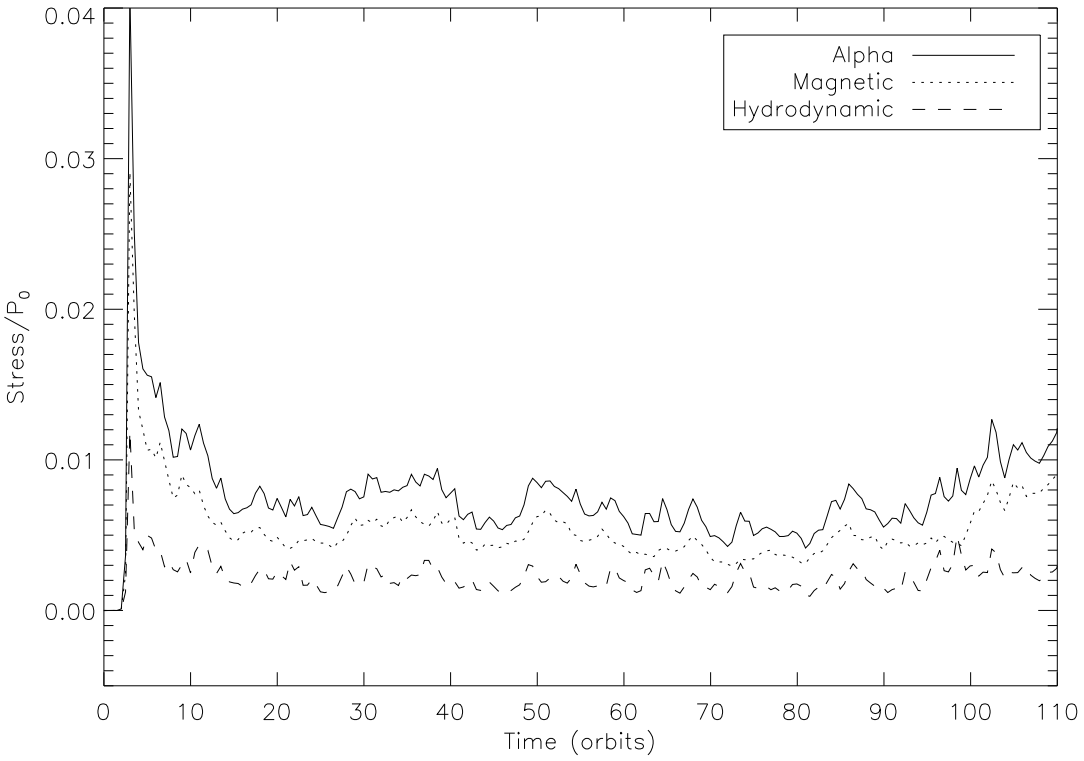

Figure 1. Time evolution of the stresses in the local disc model. The stresses are normalized to the initial gas pressure. The sum of the magnetic and hydrodynamic stresses (solid line) provides an estimate of the viscous α parameter, whose average value is 8×10^{-3}.

$$v_{\rm rel} \sim \frac{u}{\tau} |t_{\rm s_1} - t_{\rm s_2}| \qquad (7)$$

where u and τ are the velocity and lifetime of the smallest eddy, respectively.

A similar calculation as that of Fig. 3 is presented in Fig. 4, but for pairs of particles with different stopping times. Each symbol represents a different pair of stopping times (the error bars have been ommited for clarity, but give an uncertainty of $\sim 10\%$ for the data represented by the plus signs, the diamonds and the triangles, and of $\sim 5\%$ for the filled circles). The relative speeds do not decrease as steeply with decreasing separation as in the case of like particles. Again, from the order-of-magnitude estimate (7), $v_{\rm rel}$ should acquire a finite value in the limit of small stopping times. For the particles considered, this value is a significant fraction of the sound speed ($\sim 12 - 15\%$).

It is worthwhile to point out that as the inter-particle separation decreases, the effects of numerical resolution may become important for the purpose of calculating the relative velocities. The size ℓ of the smallest turbulent eddies, to which the smallest particles are coupled, varies with viscosity ν as $\ell \sim \nu^{3/4}$. The viscosity in turn can be affected by the grid resolution (HGB).

3.4 Spatial distribution

In order to improve the statistics of particle counts, we have taken as the unit of volume a group of $3 \times 3 \times 3$ grid cells, referred to as a 3-macrocell. In this way, the average occupation number is 100 particles per 3-macrocell, with an associated standard deviation of 10%.

The placement of the dust particles in the shearing box, at time t=10 orbits, is random, and therefore follows a Poisson distribution. This may no longer be true at subsequent times, when the turbulence has mixed the particles in such a way that the initial stochastic distribution has been lost. This situation is apparent in Fig. 5, where the left panel shows the cumulative distribution function, as a solid line, of the particle number n per 3-macrocell at the moment when the particles are introduced in simulation set B, for the $\Omega t_{\rm s}$=2 case. The dotted line is the corresponding cumulative Poisson distribution with the same mean ($\langle n \rangle$=100) as the n distribution. The two are alike, indicating that the initial particle positions are indeed drawn from a random sample. However, the right panel, which corresponds to t=30 orbits, makes it evident that the spatial distribution of the particles deviates from a Poisson distribution. The vertical dashed line in each panel indicates the point at which the distance d between the two distributions is greatest. This distance constitutes a measure of the deviation of one data set from the other. In the particular case shown in Fig. 5, at t=10 orbits the maximum distance is d=0.026, whereas at t=30 orbits, d=0.55. The situation is similar at all other

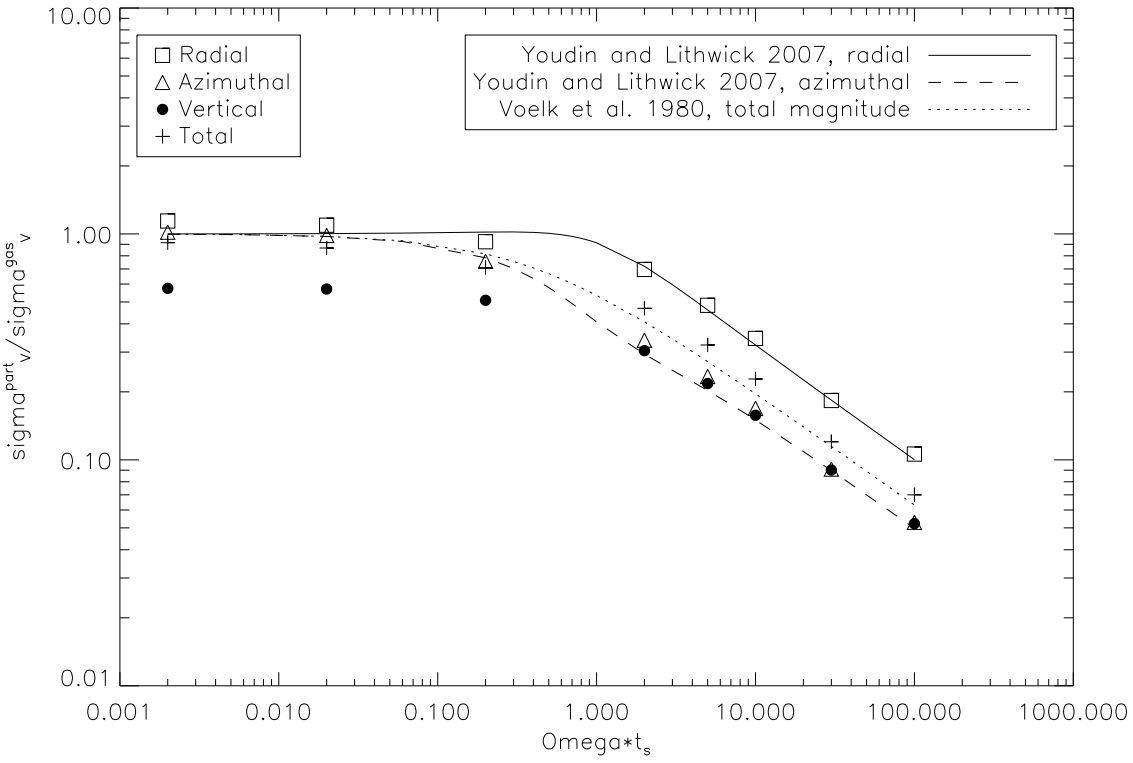

Figure 2. Ratio of particle to gas velocity dispersion, as a function of particle stopping time. Data shown correspond to the radial (*squares*), azimuthal (*triangles*) and vertical (*circles*) components of velocity, as well as to the velocity magnitude (*plus signs*). The curves represent analytical models derived for isotropic turbulence.

times $t > 0$, and for the three other hydrodynamic couplings of set B.

To measure the amount of solid particle clumping in the shearing box, we calculate the number of particles in each macrocell and divide by its mean:

$$C \equiv \frac{n}{\langle n \rangle} \tag{8}$$

Fig. 6 shows distributions of C for each particle-gas coupling, at t=20 orbits. These distributions are typical throughout the duration of the simulation. Also shown for comparison is the distribution of gas clumping, $\rho_{\rm g}/\langle\rho_{\rm g}\rangle$. Notice that the solids exhibit more over-densities with respect to the mean ($\langle C \rangle = 1$) than under-densities, showing a considerably high number of macrocells that have values of C above the average occupation number $\langle n \rangle$. The highest C attained is $C_{\rm max}$=26.5, by the particles with $\Omega t_{\rm s}$=0.125, at t =27.1 orbits. A history of $C_{\rm max}$ is plotted in Fig. 7, where the time axis has been shifted to the instant at which the particles are introduced.

The time-averaged C distributions are shown in Fig. 8. Note the difference in the shapes of the distributions compared to those in Fig. 6, particularly for $\Omega t_{\rm s}$ = 0.2, 0.125 and 0.05 at C = 0. This can be understood by considering that the time-averaging procedure effectively assigns a non-zero number of particles to each 3-macrocell, which at a specific snapshot (but not all) is likely to be empty. The non-Poissonian character of the particle spatial distribution is also evident in Fig. 8, as the distributions possess appreciable "tails" extending in the direction of increasing C. This is normally associated with spatial correlations in a system of particles in which their positions are not statistically independent (Landau & Lifshitz 1980). In the case of particles immersed in turbulence, these correlations arise from the intermittency of turbulent mixing. The correlations are manifested by an increase in the variance of the particle counts, with respect to a purely random distribution.

Positive correlations can induce clustering at some range of spatial scales. One way to quantify this clustering is by means of the pair correlation function

$$\eta(\Delta r) = \frac{\langle n(r) n(r+\Delta r) \rangle}{\langle n(r) \rangle^2} - 1 \tag{9}$$

where the particle number density n is evaluated at two points separated by the distance Δr. The measurement of this quantity is common in the study of cloud droplet clustering in the presence of turbulence in the Earth's atmosphere (Kostinski & Jameson 2000). In order to calculate η for the population of solids in our shearing box, we proceed as follows. Given the anisotropic character of the turbulent eddies present in the box (HGB), η is measured independently along each spatial direction i (=1,2,3, or x, y, z):

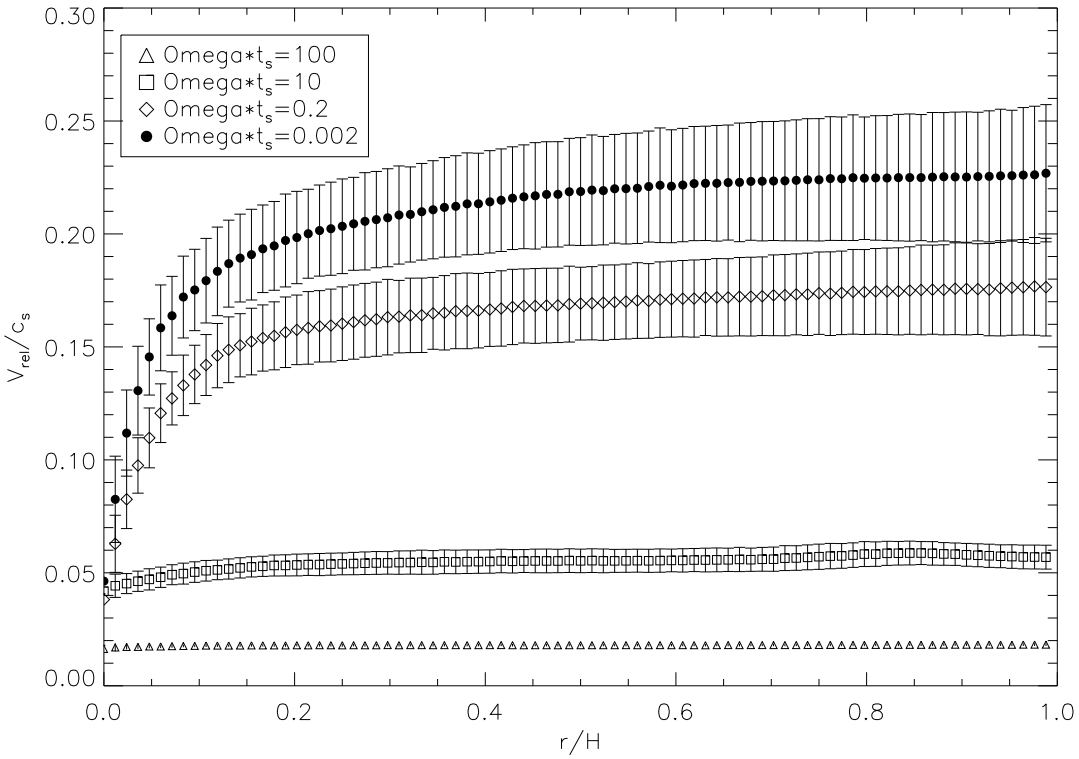

Figure 3. Relative speed (in units of the sound speed) as a function of inter-particle separation (in units of scaleheight), for pairs of particles with the stopping times shown on the upper left-hand corner. The number of particles per stopping time is 700. Data have been binned with respect to r, with a bin size equal to the size of a grid cell in the x direction ($\approx 0.01H$). The values of $v_{\rm rel}$ decrease with small values of the separation.

$$\eta_i(\Delta x_i) = \frac{\langle n(x_i) n(x_i + \Delta x_i)\rangle}{\langle n(x_i)\rangle^2} - 1 \qquad (10)$$

Furthermore, to obtain a sufficient number of points along each direction, at which to evaluate n, we consider 2-macrocells instead of the 3-macrocells used to calculate the clumping factor C. To avoid the effect of the periodic boundary conditions in the y and z directions, as well as the quasi-periodic conditions along the radial direction x, the separation Δx_i between 2-macrocells is constrained to be, at most, half of the corresponding box length. Thus, for example, to evaluate η_x at separations of one macrocell, a horizontal row of grid cells is chosen, say one with end cells at $x = -0.5$ and $x = 0.5$, and with fixed y and z coordinates. The particle number density n is measured at the first 2-macrocell in this row, and also at the next macrocell. The product of these two values of n is stored, and the process is repeated starting at the second macrocell. If m is the number of 2-macrocells in the row, the process ends with the product of n evaluated at macrocells $m/2 - 1$ and $m/2$. The average of all the products is calculated and inserted in the right-hand side of Eq. (10).

The row of grid cells used in the calculation just described is located at specific y and z, and it is only one of $84 \times 180 = 15,120$ similar horizontal rows. With this number of values for $\eta_x(\Delta x)$, an average over all rows at all y and z gives the volume-averaged pair correlation function $\langle \eta_x(\Delta x)\rangle$. The functions $\langle \eta_y(\Delta y)\rangle$ and $\langle \eta_z(\Delta z)\rangle$ are obtained in an analogous manner.

The volume-averaged pair correlation functions for the $\Omega t_{\rm s}$=0.05 particles, at the time of their introduction in the flow ($t = 10.0$ orbits), are identically zero, reflecting the statistical independence of the initial particle numbers. This also holds for the cases $\Omega t_{\rm s}$=0.125, 0.2 and 2. The measured $\langle \eta_i\rangle$ at the end of the simulation are shown in Fig. 9. The columns correspond to the x, y and z directions, and the rows represent, from top to bottom, the stopping times $\Omega t_{\rm s}$ =2, 0.2, 0.125 and 0.05. The error bars correspond to the data dispersion at each separation Δx_i.

One feature is immediately noticeable from Fig. 9: the vertical correlation function (third column) is very nearly flat for the four values of $\Omega t_{\rm s}$. This would seem to indicate that particles remain almost evenly mixed in the vertical direction, without deviating much from the initial random distribution. The particles show concentrations over radial distances of approximately $0.1H$ (for $\Omega t_{\rm s}$=2) and $0.05H$ (for the other stopping times). In the azimuthal direction the respective correlation lengths are $\approx H$ and $\approx 0.3H$. This range of distances represents between 5% and 16% of the box size.

The largest correlation lengths belong to the $\Omega t_{\rm s}$=2 particles, which also show the lowest average concentration (Figs. 7 and 8). Even taking the highest value of $C_{\rm max}$ for

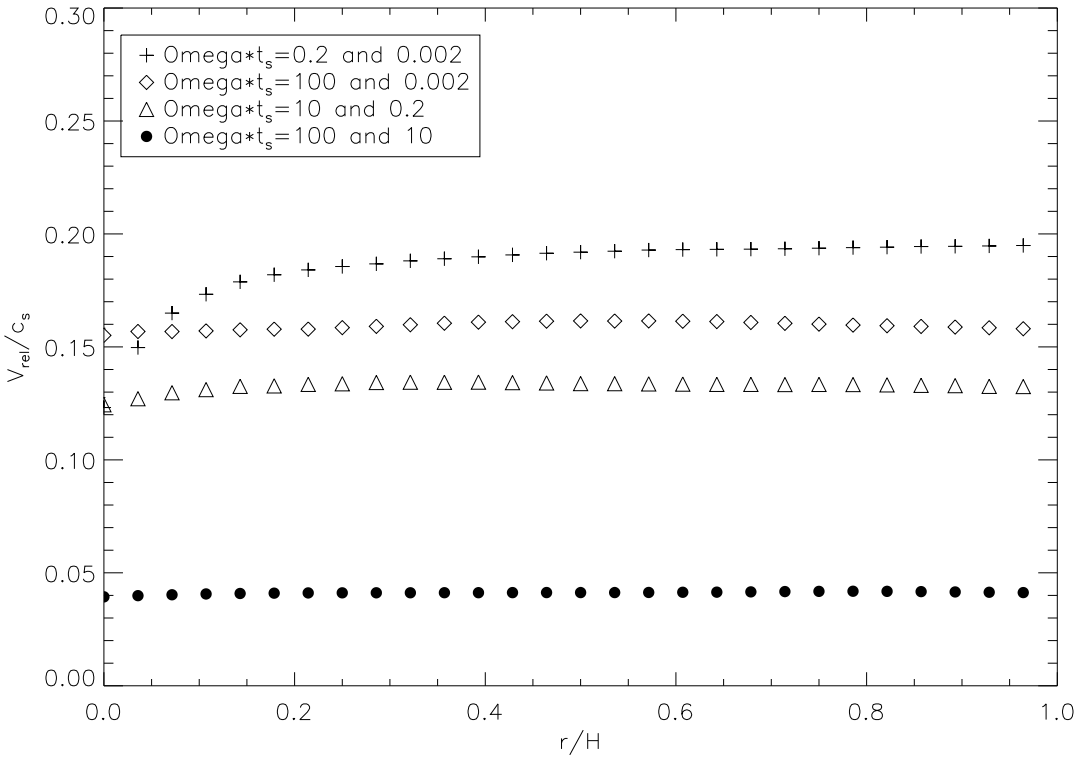

Figure 4. Same as Fig. 3, but for pairs of particles with different stopping times.

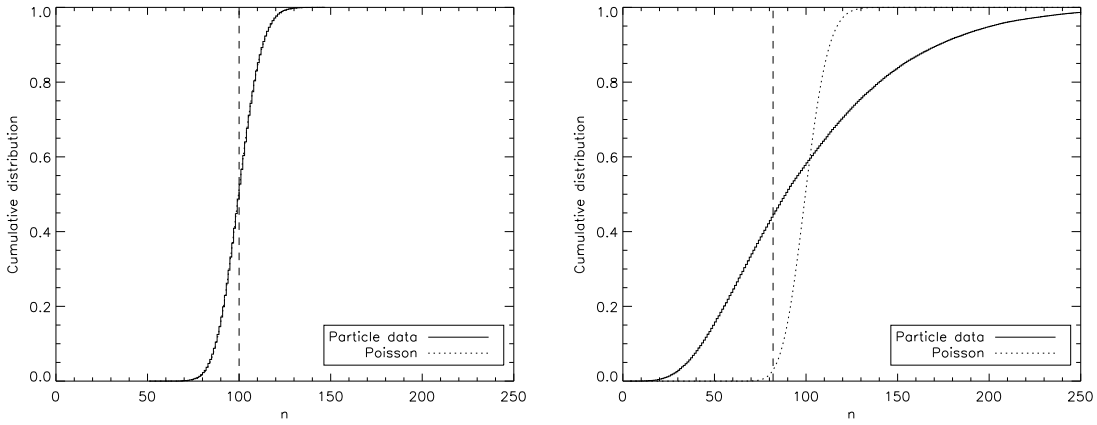

Figure 5. Cumulative distributions of the number of particles per 3-macrocell, for $\Omega t_{\rm s} = 2$. The left panel represents the initial distribution at t=10 orbits. The solid line corresponds to the particle distribution n, while the dotted line is the corresponding Poisson distribution with the same mean. The vertical dashed line indicates the value of n at which the vertical separation d between the two distributions is greatest. The right panel shows that the particle distribution is not Poissonian at t=30 orbits. This is true in general for $t >$0 and the three other values of $\Omega t_{\rm s}$.

this stopping time (≈21), the surface density reached in a clump of dimensions $\langle \eta_x \rangle \times \langle \eta_y \rangle$ is $\approx 2.1 \times 10^4 H^{-2}$, compared to $2.65 \times 10^5 H^{-2}$ for the most highly concentrated particles, those with $\Omega t_{\rm s}$=0.125.

In order to constrain the lifetime of typical particle associations from the simulation data, it is necessary to refine the working definition of a clump. Here a clump is understood to be a group of particles that has a size smaller than the length δ of the diagonal of a 3-macrocell. The size of the group is determined by calculating a clump "diameter", based on the maximum and minimum values of the particle coordinates.

For each value $\Omega t_{\rm s}$=0.2, 0.125 and 0.05, the clump with the highest particle density was followed during subsequent

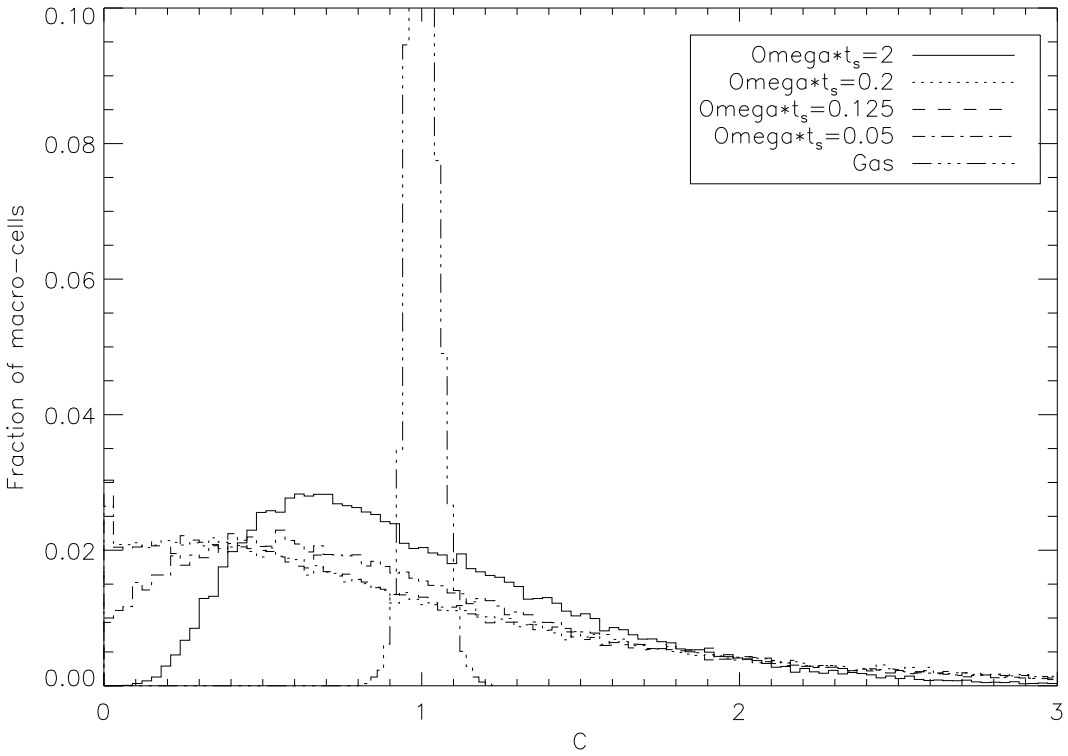

Figure 6. Distribution of the clumping number $C \equiv n/\langle n \rangle$ at t =20 orbits, for all particle stopping times. All solids exhibit an overabundance of 3-macrocells for which n is larger than the mean. All stopping times are more clumped than the gas (*dash-tripple dotted line*).

snapshots. In all cases, the particles become detached from the original clump after $\Delta t = 0.1$ orbits, in such a way that a calculation of the new diameter yields a value larger than δ. The fact that Δt is the interval between snapshots indicates that the lifetimes are less than what is possible to probe using the available data. The situation is similar if by clumps it is meant groups with horizontal dimensions corresponding to the particle correlation length.

4 DISCUSSION

The measurement of solid particle velocity dispersions in MRI turbulence allows to test the analytic model of Völk et al. (1980) and Cuzzi et al. (1993), which adopted a Kolmogorov energy spectrum. The turbulence that develops in the shearing box setup that we use follows roughly a Kolmogorov scaling (HGB), and the dispersion of the particle velocity *magnitude* is generally consistent with the previous results.

The radial and azimuthal velocity dispersions were found to conform to the analytical results of Youdin and Lithwick (2007), who use a turbulence model in which gas velocity correlations $\langle v_x v_y \rangle$ are weak compared to $\langle v_x^2 + v_y^2 \rangle$. This is indeed the case in the MRI-generated turbulent flow present in our shearing box.

Recent analytical calculations have provided closed-form expressions for the relative velocity between solids of different sizes, as a function of stopping time, in isotropic turbulence (Ormel & Cuzzi 2007). Those results validate the use of Eq. (7) in a regime where the stopping times of both particles are smaller than the lifetime τ of the smallest eddies. From a measurement of the correlation time of the gas velocities, we find $\tau \sim 0.1$ orbits. Therefore, Eq. (7) will not apply to all the stopping times shown in Fig. 4, since the stopping times for the $\Omega t_{\rm s}$=10 and $\Omega t_{\rm s}$=100 particles are, respectively, $\sim$1.6 and $\sim$16 orbits. Nevertheless, a separate calculation shows that relative velocities between pairs of the three smallest stopping times ($\Omega t_{\rm s}$=0.002, 0.02 and 0.2, which correspond to $\sim 3\times10^{-4}, 3\times10^{-3}$ and 3×10^{-2} orbits) are well described by Eq. (7) at short separations, with the lowest velocity ($v_{\rm rel} \approx 0.09 c_s$) corresponding to pairs with $\Omega t_{\rm s}$=0.002 and 0.02.

For $t_{\rm s} > t_L$, with t_L being the overturn time of the largest eddies (typically taken as one orbital period), the model of Ormel & Cuzzi (2007) gives

$$v_{\rm rel}^2 = v_{\rm gas}^2 \left(\frac{1}{1+\Omega t_{\rm s_1}} + \frac{1}{1+\Omega t_{\rm s_2}} \right) \qquad (11)$$

where $v_{\rm gas}$ is the velocity of the turbulent flow, and it is assumed that $t_{\rm s_1} > t_{\rm s_2}$ whitout loss of generality. Direct measurement from our simulation data yields $v_{\rm gas} \approx 0.12 c_{\rm s}$, and so for the two largest stopping times studied ($\Omega t_{\rm s}$=10 and $\Omega t_{\rm s}$=100) we obtain $v_{\rm rel} \approx 0.04 c_{\rm s}$, in close agreement with the numerical results of Fig. 4 (filled circles).

The two-point correlation function calculated in Section 3.4 gives an estimate of the length scale over which

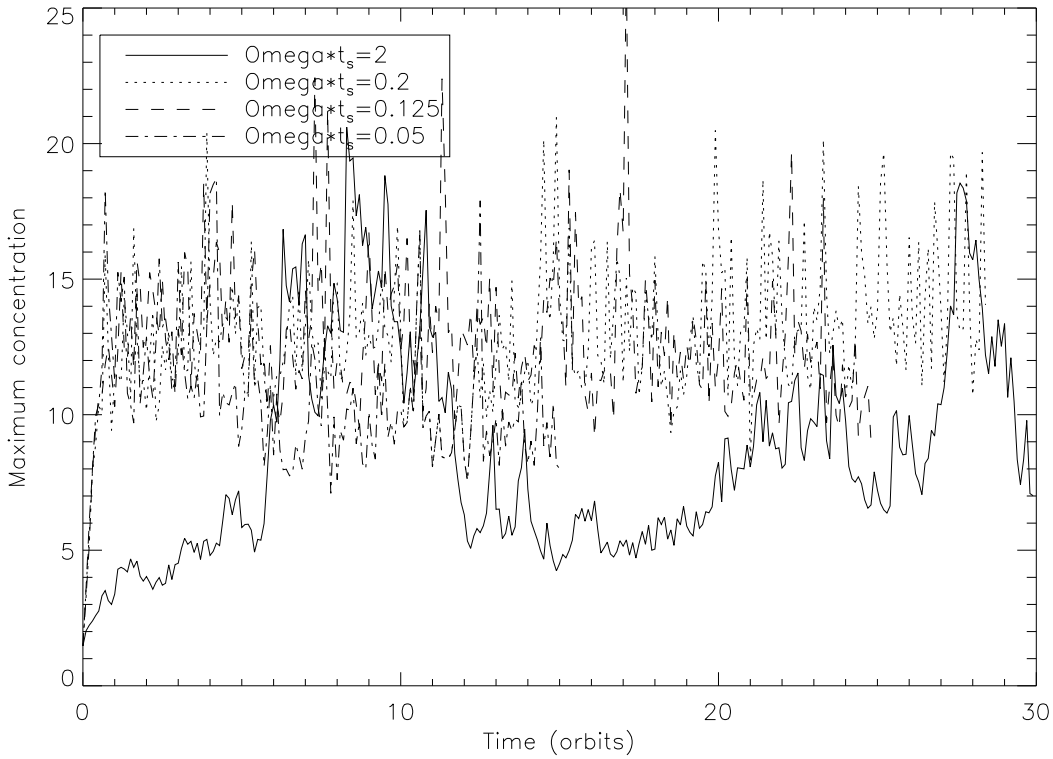

Figure 7. Time history of the maximum clumping factor $C_{\max}$ for the particle stopping times used in run B. The time marked as $t = 0$ orbits corresponds to the instant at which particles are introduced in the flow.

particle clustering occurs. In a MMSN scenario at 5 AU, in which the scale height H of the disc is $\sim 4 \times 10^{12}$ cm, the minimum correlation length of the particle number density would be $\xi \sim 0.05H \sim 2 \times 10^6$ km. A recent model of chondrule formation, in which molten chondrules come to equilibrium with the gas evaporated from other chondrules, indicates that these particles must have originated in regions larger than 6,000 km in radius, or $\xi \sim 6 \times 10^{-4} H$ (Cuzzi & Alexander 2006). The smallest particles in our study of the spatial distribution correspond roughly to solids with a radius of 20 cm, two orders of magnitude larger than typical chondrule sizes. It would be necessary to perform additional calculations with particle stopping times that correspond to this size range, in order to further constrain the value of ξ. However, it is unlikely that current computational resources would allow for the necessary resolution to probe such small correlation lengths.

We have estimated the Jeans radius R_J of the maximally concentrated clump for each stopping time, following calculations by JKH. Using similar disc parameters (column density $\Sigma = 900$ g cm^{-2}, average dust-to-gas density ratio $\zeta = 0.01$, and scale height-to-radius ratio $H/r = 0.04$) and a turbulent diffusion coefficient $\delta_{\rm t} = \alpha = 8 \times 10^{-3}$ inferred from our shearing box model, the values of R_J are smaller than the typical clump size by factors between $\sim$9 and $\sim$250. The clump radius that is closest to R_J corresponds to the $\Omega t_{\rm s}$=2 particles. Under these assumptions, our dense particle associations would not be subject to a gravitational collapse.

Even though the stopping times used in this calculation and those studied by JKH are different, we can still compare our results for $\Omega t_{\rm s}$=2 with their $\Omega t_{\rm s}$=1 case. The main difference resides in the particle velocity dispersion, which we measure as $0.036 c_{\rm s}$, approximately 50% larger than they obtain. If our maximally concentrated $\Omega t_{\rm s}$=2 group were to be gravitationally unstable, the velocity dispersion would need to be a factor ~ 2.5 smaller. We also note that the radial drift incorporated by JKH leads to particle concentrations that are stronger than in the cases presented here (Johansen et al. 2007), making gravitational collapse more likely.

5 CONCLUSIONS

We have performed numerical MHD calculations of solid particle velocities and spatial distribution in a turbulent protoplanetary disc, in the context of the shearing box model. The results suggest that, even though the turbulent flow has an anisotropic spectrum, the dispersion of the particle velocity magnitude (normalised by the corresponding dispersion for the gas) as a function of particle stopping time is consistent with analytical models that assume isotropy. Nevertheless, the dispersions of the individual velocity components for each stopping time are different. In the case of particles with $\Omega t_{\rm s} \gtrsim 1$, the radial component of the solid-to-gas velocity dispersion ratio is larger than the azimuthal and vertical components typically by factors of $\sim 2.3-\sim 2.5$. The relative speed between pairs of particles with the same stopping time decreases towards small values at small

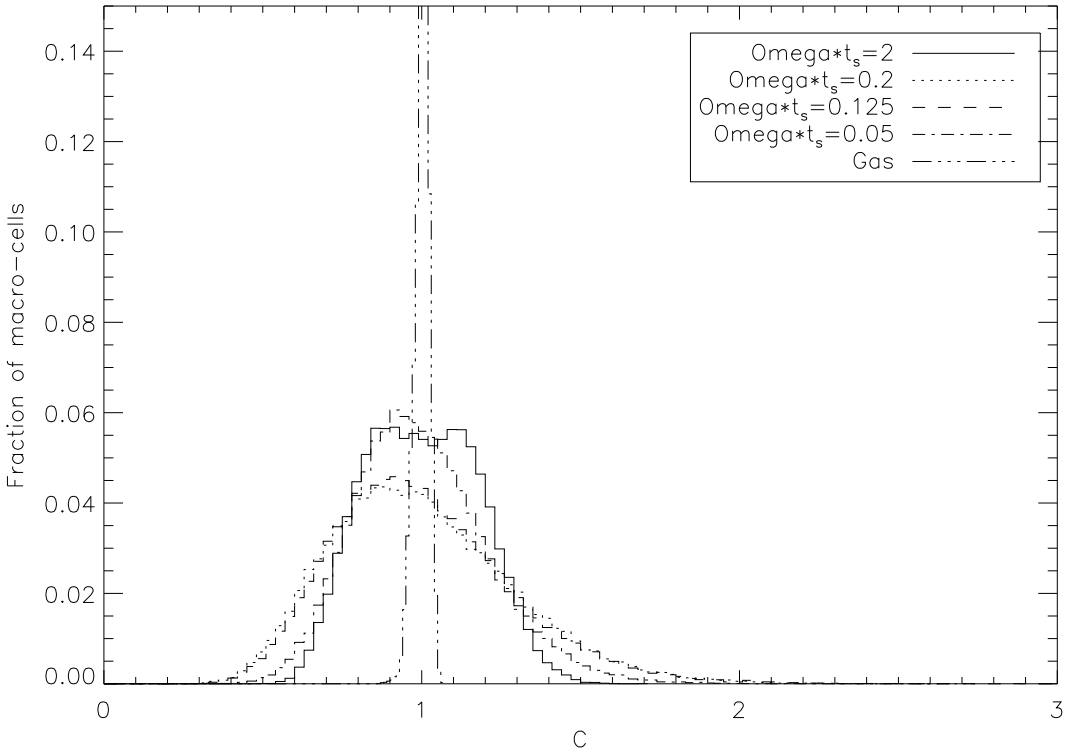

Figure 8. Time-averaged distribution of the clumping number C, for all particle stopping times. The tails of the distributions, although not particularly long, are indicative of the non-Poissonian nature of the number density counts.

separations, whereas for pairs of different stopping times the relative speed reaches a finite value that depends on the sizes of the pair members.

The clustering induced on the particle spatial distribution by the turbulent flow gives rise to short-lived clumps. Under conditions of a minimum-mass solar nebula, these clumps are at least nine times larger than their respective Jeans radii, as a result of high particle velocity dispersions. Gravitational collapse would therefore seem to be an unlikely mechanism in the formation of more massive objects, under the conditions that we assumed.

Future calculations should increase the numerical resolution used in the measurement of the relative velocities between particles, in order to improve fittings to existing analytical models.

ACKNOWLEDGMENTS

This work benefited from discussions with Jim Pringle, Richard Nelson, and Gordon Ogilvie. Suggestions from an anonymous referee were most valuable. AC acknowledges support from CONACYT scholarship 167912 and a Caltech Postdoctoral Scholarship. Part of this work was carried out at the Jet Propulsion Laboratory, which is operated by the California Institute of Technology under contract to NASA.

REFERENCES

Balbus S.A., Hawley J. F. 1991, ApJ, 376,214
Blum J., Wurm G. 2000, Icarus, 143, 138
Carballido A., Stone J. M., Pringle J. E. 2005, MNRAS, 358, 1055
Carballido A., Fromang S., Papaloizou, J. 2006, MNRAS, 373, 1633
Chhabra A. B., Meneveau C., Jensen V. R., Sreenivasan K. R. 1989, Phys. Rev. A, 40, 5284
Cuzzi J. N., Dobrovolskis A. R., Champney, J. M. 1993, Icarus, 106, 102
Cuzzi J. N., Dobrovolskis A. R.& Hogan R. C. 1996, *Chondrules and the protoplanetary disk*, R. Hewins, R. H. Jones, and E. R. D. Scott, eds., Cambridge University Press.
Cuzzi J. N., Hogan R. C., Paque J. M., Dobrovolskis R. 2001, ApJ, 546, 496
Cuzzi J. N. & Hogan R. C. 2003, Icarus, 164, 127
Cuzzi J. N. & Alexander C. M. O. 2006, Nature, 441, 483
Gammie C. F. 1996, ApJ, 457, 355
Hartmann L., Calvet N., Gullbring E., D'Alessio P. 1998, ApJ, 495, 385
Hawley J. F., Gammie C. F., Balbus S. A. 1995, ApJ, 440, 742 (HGB)
Johansen A., Klahr H. 2005, ApJ, 634, 1353
Johansen A., Klahr H. & Henning T. 2006, ApJ, 636, 1121 (JKH)
Johansen A., Youdin A. N. 2007, ApJ, 662, 627
Johansen A., Oishi J. S., Mac Low M., Klahr H., Henning T. & Youdin, A. 2007, Nature, 448, 1022

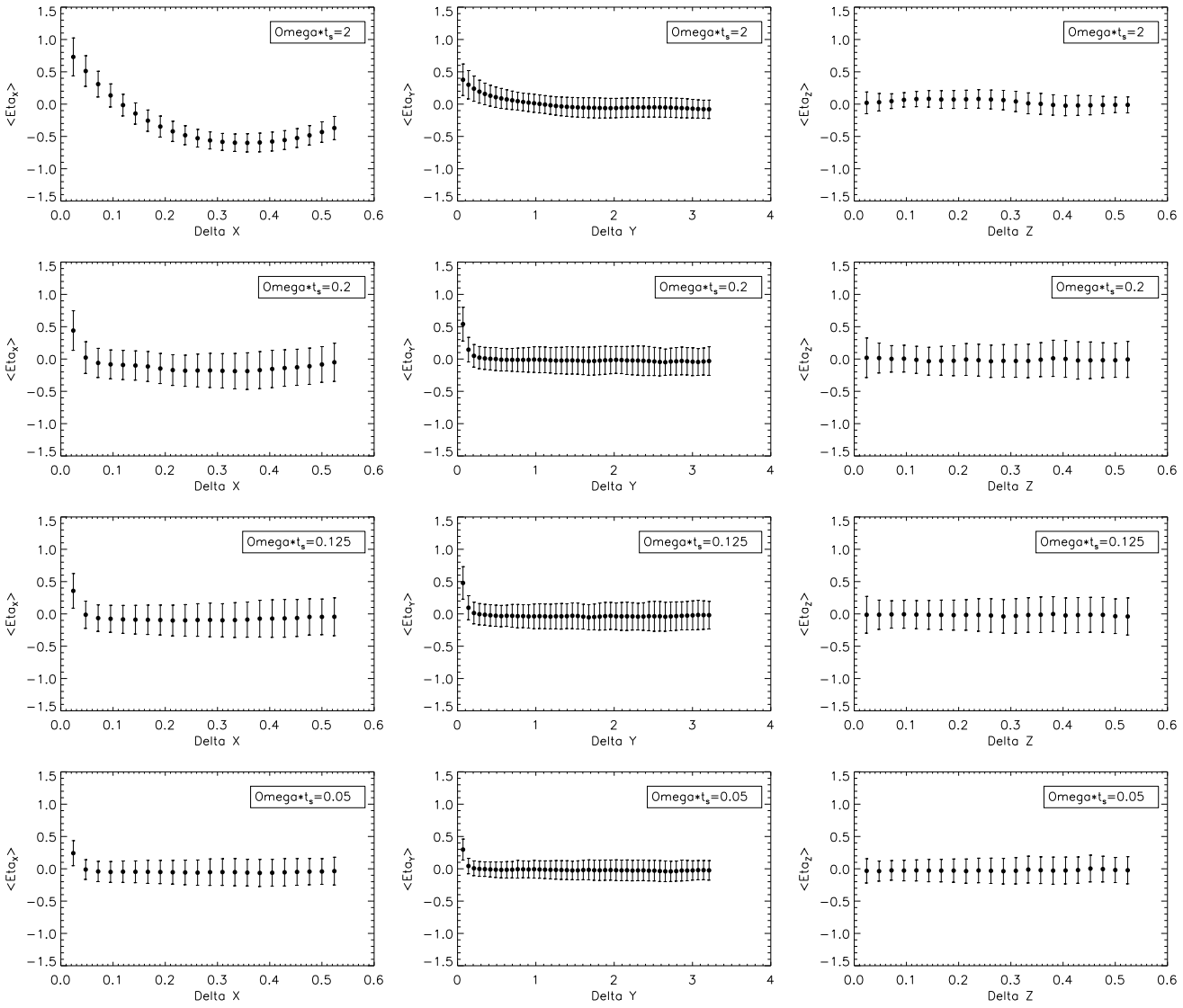

Figure 9. Pair correlation function for all particle stopping times, at the end of simulation set B. The left, centre and right columns correspond to the x, y and z directions, respectively. First row: $\Omega t_{\rm s} = 2$; second row: $\Omega t_{\rm s} = 0.2$; third row: $\Omega t_{\rm s} = 0.125$; fourth row: $\Omega t_{\rm s} = 0.05$. The vertical correlation functions are very nearly zero, indicating that particles are evenly mixed in that direction.

Kostinski A. B. & Jameson A. R. 2000, J. Atm. Sci., 57, 901
Landau L. D. & Lifshitz E. M. 1980, *Statistical Physics*, Pergamon Press, 687 pp.
Maxey M. R. 1987, J. Fluid Mech., 174, 441
Ormel C. W., Cuzzi J. N. 2007, A&A, 466, 413
Press W., Teukolsky S.A., Vetterling W. T., & Flannery B. P. 1992, *Numerical Recipes in Fortran 77*, Vol. 1, Cambridge University Press, second edition
Sano T., Miyama S. M., Umebayashi T. & Nakano T. 2000, ApJ 543, 486
Stone J. M., Norman M. L. 1992a, ApJS, 80, 753
Stone J. M., Norman M. L. 1992b, ApJS, 80, 791
Völk H. J., Morfill G. E., Röser S., Jones F. C. 1980, A&A, 85, 316
Weidenschilling S. J. 1977, MNRAS, 180, 57
Weidenschilling S.J. 1984, Icarus, 60, 553
Youdin A. N., Goodman J. 2005, ApJ, 620, 459
Youdin A. N. & Johansen A. 2007, ApJ, 662, 613
Youdin A. N., Lithwick Y. 2007, Icarus, 192, 588